Available online at www.sciencedirect.com
SCIENCE DIRECT®
Journal of Sound and Vibration 282 (2005) 341–366
JOURNAL OF SOUND AND VIBRATION
www.elsevier.com/locate/jsvi

Laser vibrometry technique for measurement of contained stress in railroad rail

Vesna Damljanović, Richard L. Weaver*

Department of Theoretical & Applied Mechanics, University of Illinois at Urbana-Champaign, Urbana, IL 61801-2983, USA

Received 2 September 2003; accepted 22 February 2004

Abstract

Based on the known sensitivity of a beam's effective flexural rigidity to its static axial load, we experimentally investigate whether measurements of lateral bending wavenumber, at a specified imposed frequency, can be used to nondestructively determine that load. Initial estimates are that at an imposed frequency in the vicinity of 200 Hz, where wavelengths are of the order of 2 m, the sensitivity should be adequate if the wavenumber can be extracted with sufficient precision. Scanned laser vibrometry, followed by digital lock-in, and referencing with a fixed accelerometer, is found to accurately measure steady-state vibration distributions. Nonlinear least-square fits to theoretical forms consisting of a sum of guided vibration modes then give a best-fit value for that wavenumber, a value that correlates well with the known levels of load in the experiments. The proposed technique appears viable.

1. Introduction

With the advent of continuously welded rail in the last few decades, in which a rail can continue for miles without interruption, the railroad industry has experienced an increasing concern with large contained loads due in part to constrained thermal expansions and contractions. There has long been a desire for efficient nondestructive and accurate methods to assess those loads [1]. With

*Corresponding author. Tel.: +1-217-333-3656; fax: +1-217-244-5707.
E-mail address: r-weaver@uiuc.edu (R.L. Weaver).

0022-460X/$ - see front matter
doi:10.1016/j.jsv.2004.02.055

neutral temperature, T_0, defined as the temperature at which the stress is zero, one calculates that the contained compressive load is given by $P = \alpha EA(T - T_0)$, where α is the coefficient of thermal expansion, E is the Young's modulus and A is the cross-sectional area. For typical rails, αEA is about 2500 lbf/°F.

A variety of techniques have been proposed for the efficient assessment of contained load (or of neutral temperature, which is much the same thing). Accuracies of at least 10°F in neutral temperature, or 25 kips in contained load, are required. X-ray diffraction can measure absolute strain, but X-rays penetrate only the surface. Magnetic hysteresis is similarly dependent only on surface properties. Ultrasonic acousto-elasticity [2,3] is highly challenging, in part due to the weak acousto-elastic constants of steels, in part due to the competing effects of material texture, and in part due to its sensitivity to only the region being insonified. Permanently attached strain gages [4] are used in places, but require a reference state, and do not correct for plastic creep.

Rail-uplift [5] is increasingly proposed as a cost-effective technique. Some 30 m of rail is detached from the fasteners and the vertical force needed to lift the center by a fixed amount is measured. Large tension leads to greater effective bending rigidity, and can be detected as a greater required force. It is a testimony to the importance of the problem that the industry is willing to engage in such a cumbersome process.

Vibration techniques have also been proposed. In a series of reports Beliveau and co-workers [6,7] investigated a proposal to compare resonant frequencies of beams with and without contained load, and correlate changes with that load. Much as with rail-uplift, tension corresponds to greater effective rigidity, and higher resonant frequencies. Unfortunately, resonant frequencies are more sensitive to the natural variations in supports and boundary conditions than they are to contained load, and the technique was not sufficiently reliable.

2. Proposed stress measurement technique

Here, we investigate a variation on the resonant frequency approach discussed by Livingston et al. [6]. Like the resonant frequency technique, and like the rail uplift technique, it takes advantage of the sensitivity of bending rigidity to contained load. Unlike the resonant frequency technique which uses the amplitude of vibrations, it measures the wavenumber of the spatial distribution of vibration amplitude in response to imposed dynamic loads at a fixed frequency. It is proposed to drive a rail in situ, at a fixed frequency chosen for convenience, to then measure the wavenumber ($k_{\text{lat.bend.}}$) of the resulting lateral bending waves, and finally to compare this with the $k_{\text{lat.bend.}}$ expected without stress. The difference is the quantitative indicator of contained load, the formula for which is given below. Unlike the resonant frequency approach, which is contaminated by the unknown influence of rail supports, the proposed technique is in principle independent of them. While the amplitude of response is of course dependent on the global condition of the rail and its supports and in particular the length of a free unsupported span, the wavenumbers of the guided waves over a short unsupported span depend only on the condition of the rail in that span. Thus, no modelling of supports is needed for the proposed technique, their only influence being to modify the amplitudes of the many modes, all duly considered as explained below. This section begins with a brief review of the physical principle as revealed by a simple Euler–Bernoulli model

of rail bending. It then describes the proposed measurement procedure in more detail. It discusses the principles and challenges, and the method for the extraction of lateral bending wavenumber from scanned laser vibrometry measurements.

2.1. Euler–Bernoulli estimate for required precision

A strength-of-materials model—the well-known Euler–Bernoulli beam theory—while accurate only at long wavelengths, nevertheless gives a good indication of the principles behind the relationship between stress and wavenumber. This theory also gives a good indication of the precisions that may be needed if the method is to be practical—in error analysis additional variations associated with the exact theory are negligible. (The Euler–Bernoulli theory is inadequate for precise predictions, so for the proposed technique, wavenumbers are calculated using elasticity theory, with precision limited only by the finite element mesh size.)

From the dispersion relation associated with the Euler–Bernoulli beam theory, for a beam of Young's modulus E, density ρ, area of cross-section A and moment of inertia I, the contained longitudinal load P is

$$P = \rho A\left(c_b^2 r_g^2 k^2 - \frac{\omega^2}{k^2}\right) \tag{1}$$

where $c_b = \sqrt{E/\rho}$ is the bar wavespeed, $r_g = \sqrt{I/A}$ is the radius of gyration and k is the lateral bending wavenumber. Error analysis of this equation (taking variations, essentially partial derivatives δP with respect to c_b, r_g and k, while recognizing that $\omega^{2\approx c_b{}^2} r_g^2 k^4$ at realistic loads P) gives the imprecision with which the contained load (or neutral temperature) is recovered:

$$\frac{\delta P}{EA} = \alpha\delta\Delta T = 2r_g^2 k^2\left(\frac{\delta r_g}{r_g} + 2\frac{\delta k}{k} + \frac{\delta c_b}{c_b}\right) \tag{2}$$

where α is the coefficient of thermal expansion. It follows that the imprecision of contained load δP (or of neutral temperature $\delta\Delta T$) has contributions from the uncertainty in rail dimensions, the imprecision of measuring the bending wavenumber k and the imprecision of determination of the rail elastic properties.

For the modified rail 136-lb AREMA (the cross-section geometry is shown in Fig. 1) with $r_g = 0.9925$ in, $E = 3.05 \times 10^7\,\mathrm{lbf/in^2}$, $\rho = 7.33 \times 10^{-4}\,\mathrm{lbf\,s^2/in^2}$, $v = 0.3$ and $\alpha = 7 \times 10^{-6}/^\circ\mathrm{F}$, and assuming the span length is equal to about one half-wavelength of the expected lowest bending wave, $L = 39$ in, with the wavenumber $k = \pi/L$, one concludes that the target precision of ± 26 kips (or $\pm 10^\circ$F) at the excitation frequency of 203 Hz can be achieved providing the compound imprecision of the three terms in Eq. (2) is not greater than 0.54%. Because these three sources of error are not necessarily in phase, it is safe to assume that the radius of gyration and the bar wave speed must each be known to at least 0.54% accuracy and the bending wavenumber k to within 0.27%, to obtain a precision close to target. If two sets of measurements for two different frequencies are used, the precisions of c_b and r_g become irrelevant because they cancel out of the two associated equations for the load precision.

In general, decreasing the scan length by a factor of n results in n^2 times lower precision of stress or neutral temperature measurement. For example, decreasing the scan length to 20 in while keeping the other parameters the same, leads to a neutral temperature precision of ± 40 F, which

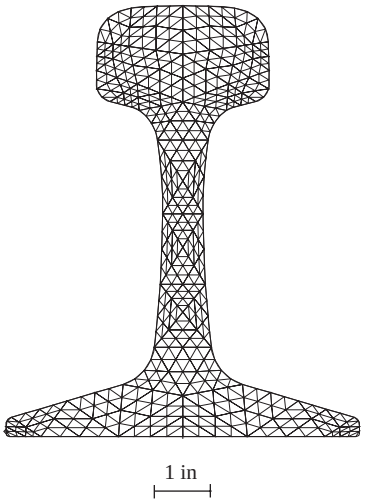

Fig. 1. The geometry and FE mesh used to model the rail 136-lb AREMA cross-section (136-lb denotes the rail nominal mass in lbm/yd). A modification of the standard US rail profile is used here.

can be compensated only by knowing r_g and c_b each to within 0.135% and k to within 0.067%. But such short lengths used in a slender beam model, bring even the calculations of the Euler–Bernoulli model into question and, therefore, should not be relied upon in the measurements. Conversely, increasing the span to 80 in causes the requirements on $\delta r_g/r_g$, $\delta c_b/c_b$ and $\delta k/k$ to be relaxed by a factor of four.

Eq. (2) may also be used to show the desired formula relating the contained load P (that is, the *difference* from the zero load) to the fractional difference between measured $k_{\text{lat.bend.}}$ and that predicted for the zero-load case:

$$P = 4EAr_g^2k^2\left(\frac{\delta k}{k}\right). \tag{3}$$

For the load range of 0–100 kips, the $P(\delta k/k)$ curve is practically linear, passing through the origin. This indicates that P is proportional to the fractional difference in $k_{\text{lat.bend.}}$ with a proportionality of 100 kips per % deviation in $k_{\text{lat.bend.}}$, for the rail 136-lb AREMA at $f = 203$ Hz where $k_{\text{lat.bend.}} = 0.0814\,\text{in}^{-1}$.

2.2. Measurement procedure

The problem of measurement of $k_{\text{lat.bend.}}$ to the required precision may well be non-trivial, especially if practical concerns limit the free span over which the fasteners can be detached for purposes of the measurement. While long spans will give greater precision, as seen above, detaching all the fasteners over long spans is undesirable in practice. Over short spans there may be contributions to the steady-state vibration field that are due to waves evanescent from the edges. Regardless of the span length, one expects contributions from other propagating guided modes, including the vertical bending, the longitudinal, and the torsional waves.

In order to solve this problem we note that the steady-state displacement field is given, to good accuracy, by a truncated guided mode sum:

$$\hat{d}(z) = \sum_{m=1}^{M} \alpha_m \upsilon_m(x, y; \omega) \mathrm{e}^{-\mathrm{i}k_m z} \tag{4}$$

where $\upsilon_m(x, y; \omega)$ is the n^{th} guided mode shape and k_n is the n^{th} wavenumber at frequency ω. Critical to the technique proposed here is the observation from waveguide theory that the steady-state harmonic response of a rail takes the above form, with constant α_m over any uniform unsupported span z of the rail [8,9]. The coefficients α_m depend on the forcing and supports and are in general difficult to predict. (They have been calculated [8] for the special case of an infinite uniform unsupported rail with a harmonic point load.) The wavenumbers, including the lateral bending wavenumber, are independent of those supports. The lateral bending wavenumber depends on the unknown contained load and is therefore uncertain. In the parameter range of interest the other wavenumbers are largely unaffected by that load. While there are infinitely many guided modes, most are highly evanescent, and may be neglected [8] (hence the truncation to only M terms) at all points z sufficiently far from the edges or supports or dynamic loads.

We propose to fit the truncated sum (4) to the measured displacement profile $d(z)$ by using values for the guided modes υ_m and wavenumbers k_n, as determined by a high-precision FEM code [9] that calculates the propagating and evanescent-guided modes of a rail. The fit procedure involves the minimization of the mean-square residual (χ^2) between the measurement and the sum in Eq. (4) with respect to variations in the wavenumber $k_{\text{lat.bend.}}$ (with all other wavenumbers fixed) and the coefficients α_m. The result is a best-fit $k_{\text{lat.bend.}}$, along with coefficients α_m that are not important. The difference between the best-fit $k_{\text{lat.bend}}$ and that expected at zero load is the quantitative indicator of contained load, as in Eq. (3).

The basic set-up for the proposed field measurement of contained stress in a railroad rail is shown in Fig. 2. The irregular distribution of fasteners is common in the field (defying efforts to model the railroad rail as a beam on periodic foundation), and is emphasized on this schematic in order to reiterate that knowledge of their position, periodicity or type of constraint is irrelevant for the determination of contained stress.

3. Experimental confirmation with known load

The accuracy and overall viability of the proposed technique were tested by applying it to a $91\frac{3}{4}$ in piece of as-received railroad rail 136 AREMA, under controlled test-bay conditions with known compressive load. The rail section was loaded axially, in compression, by a hydraulic actuator with automatic load control. To ensure the strongest dynamic response and best signals at each load level, the rail was vibrated at its corresponding resonant frequency. Two scans at different points on the rail cross-section, along a $55\frac{1}{8}$ in span in the middle, were completed for each of 5 load levels. The load was maintained constant throughout each scan. Signals were taken from both the laser vibrometer, and from a fixed accelerometer, which provided a reference. A digital lock-in process was used to minimize the influence of noise. A linear and nonlinear least residual (least χ^2) process was used to fit that measured data to the form (4). The number of terms

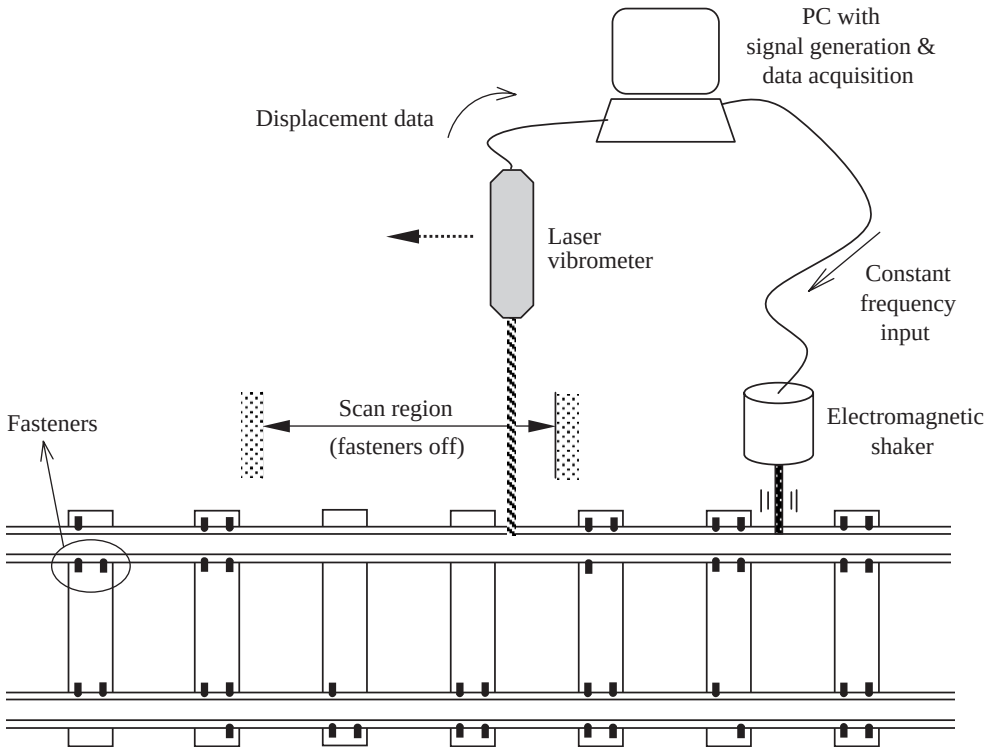

Fig. 2. Schematic of the rail stress measurement set-up in the field.

M was taken equal to 10, corresponding to 5 rightward and 5 leftward waves. Except for the wavenumber, $k_{\text{lat.bend.}}$, of the lateral bending wave, the wavenumbers used in the fit were taken from a FE solution [9]. The fractional difference between the $k_{\text{lat.bend.}}$ that minimizes the fit residual, and the $k_{\text{lat.bend.}}$ predicted by the FEM code, was plotted versus the load, and the resulting curve compared with expectations. This process is described in greater detail in the following subsections.

3.1. Measurements of rail material properties and geometry

The bar wave speed $c_b = \sqrt{E/g}$, the major material parameter that features in our model, was indirectly measured using longitudinal vibrations excited by an axial tap at one end. The laser vibrometer was focused axially on the other end and the resulting signal was Fourier-transformed. The peaks in the spectrum corresponding to the natural axial frequencies of the rail were identified. These frequencies are multiples of bar wave speed divided by twice the beam length. The bar wave speed calculated from the first three axial modes was $c_b = 205\,040 \pm 480\,\text{in/s}$ (or $5126 \pm 12\,\text{m/s}$). The reported error indicates a 0.2% precision—better than the required 0.54%.

The Poisson ratio, needed in the FE code, was determined by combining that c_b with the ultrasonic wavespeed across the rail head $c_L = 237\,760 \pm 200\,\text{in/s}$ (or $5944 \pm 5\,\text{m/s}$) measured

using a 10 MHz multiply reflected ultrasonic pulse:

$$c_L = \sqrt{\frac{E}{\rho}}\sqrt{\frac{1-v}{(1+v)(1-2v)}} \quad \Rightarrow \quad v = 0.299. \tag{5}$$

That value is essentially identical to the published nominal value for carbon steel of 0.30, and the difference is found satisfactory.

Finally, the exact shape of our factory-good rail (i.e., cross-sectional area and moment of inertia, or radius of gyration r_g) was not measured. The cross-sectional outline used in the FEA was a slightly modified version of the published nominal 136-lb AREMA dimensions, which in turn accurately represents any given factory-good rail only to the limit of the tolerances prescribed by the AREMA standards. It was assumed that the nominal cross-section is acceptable because the allowed production tolerance is better than 0.4%, which is again better than 0.54% required by Eq. (2). However, the discrepancy between our FEM model and the nominal cross-section increased the total inaccuracy: the radius of gyration for the most accurate mesh used in the FEM calculations was 0.4% different from nominal, the difference being mostly due to a more tapered (thinner) rail foot (Fig. 2). The potential inaccuracy of the cross-section geometry could be remedied in the future by in situ profilometry of the cross-section.

3.2. Test-bay measurement set-up

The rail-actuator assembly was placed between two massive supports (schematics of the main part of the set-up are shown in Fig. 3): a welded steel plate structure (on the left end of the rail) and a concrete block (on the right end of rail). Both supports were attached to the test-bay floor with structural bolts and a layer of hydro-cal (gypsum) to enhance the contact between the

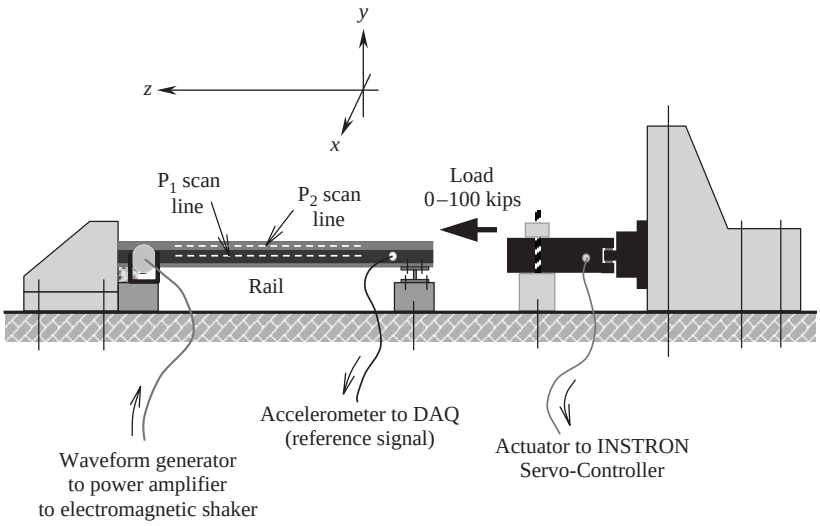

Fig. 3. Schematic of the test-bay measurement set-up (laser vibrometer scan platform and signal processing instrumentation are not shown).

concrete bloc and the floor, ensuring no slip and the rigidity of the supports even at the maximum applied load of 100 kips.

An MTS Model 204.81 hydraulic actuator was used to axially load the rail with up to 100 kips in compression. A constant load level was maintained by an INSTRON 8500 servo-controller, via a servovalve integrated in the actuator, with a closed-loop position feedback from the load cell placed in the piston head. The load cell used here was a strain-gage-based transducer with sensitivity of ± 0.01 kips. The actuator was bolted at one end to the concrete block and its vertical swivel axis was fixed after aligning with the rail. At its other end, the actuator was constrained vertically as well as laterally by a steel block bolted to the floor.

The rail was laid on a foam pad at its left end, with a sheet of lead between it and the vertical wall of the welded steel support, to prevent slipping. At the loading end, the rail was bolted to a custom-made steel I-profile, which was bolted to a small steel block that was in turn bolted to the floor. The I-profile ensured that the rail does not shift vertically or laterally during loading, but only axially. This constraint was necessary because the neutral axis of the rail could not be rigorously maintained collinear with the loading axis, causing the rail to shift upwards and sideways even at low loads. All contact surfaces in the rail-actuator-supports assembly were machined with 1° perpendicularity tolerance. The actuator axis was aligned with the central axis of the rail with maximum 1° of discrepancy from the horizontal. The dimensions of the I-profile itself were determined from the desired compliance in the axial direction, employing strength-of-materials bending theory—not more than 1 kip in 100 kips was allowed to be 'lost' in axial rail contraction of 2.3×10^{-2} in (the amount of deflection of the I-profile at 100 kips). The load was transferred to the rail by the adaptor—a simple steel cylinder that can be screwed on the actuator piston (that is, the load cell) on one end, and that has a deep flat notch on the loading end, wide enough to fit the web of the rail profile without touching its sides.

A 12.5 lbf electrodynamic shaker (Labworks Inc.) was used to excite the rail at a constant frequency. An ICP® accelerometer (PCB Piezotronics Inc.), with quartz sensing element and shear sensing geometry and with ± 50 g measurement range, provided the fixed reference that could be compared with the signal from the scanning vibrometer. Standard procedure was employed for attaching the shaker and accelerometer [10]: a small strong magnet maintained contact between the shaker stinger and the rail surface, ensuring that the vibration response is clean from nonlinearities induced by beating of the stinger. The shaker was placed near the support end of the rail. A small amount of petro-wax was used to attach the accelerometer to the rail surface near the loading end of the rail. The accelerometer and the shaker were fixed close to the rail ends, both outside the scan region.

The scans were performed in the positive direction of the z axis shown in Fig. 3. The scan platform consisted of a pine board, a metric ruler affixed at its edge and the aluminum tracks on which the polyethylene plate with a position marker (Fig. 4) could slide, carrying the post-and-bracket assembly for the vertical positioning. The laser vibrometer was fixed on top of the bracket that could smoothly slide along the vertical post and be fixed at a prescribed height. The entire scan platform was placed on a suitably low table topped with two layers of high-density foam in order to insulate the laser vibrometer from the rail vibrations.

Much attention was given to alignment of the scan platform with respect to the rail. The platform was aligned manually in the horizontal plane for every scan; this procedure resulted occasionally in noticeable measurement errors. The vertical alignment was completed only once

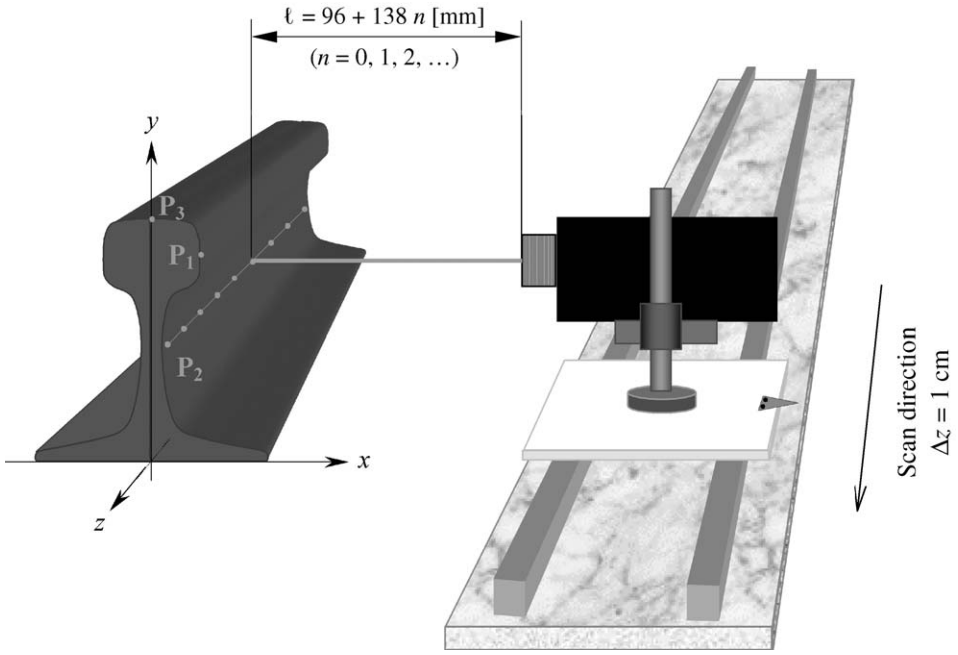

Fig. 4. Scan platform and vibrometer positioning with respect to rail (ℓ is one of the laser visibility maxima).

and remained on that level for all the scans, but the laser vibrometer stand-off distance had to be adjusted every time when changing from P_1-scan to P_2-scan and vice versa, because the x coordinates of P_1 and P_2 are different. This adjustment was necessary in order to ensure that the same laser beam length (at one of the visibility maxima, ℓ) was used in both scans and over the entire scan length; the entire table was moved towards or away from the rail.

The rail response was scanned in 1 cm steps by a Polytec PDV 100 portable digital vibrometer with a He–Ne laser ($\lambda = 633$ nm) of 50 μm spot size and better than 0.05 μm/s resolution when operated in its 20 mm/s measurement range. The analogue voltage output of the vibrometer is then sent to the data acquisition system.

In addition to maintaining the constant beam length (stand-off distance), signal quality was enhanced by focusing the laser prior to each scan. The greater the beam length, the more difficult it is to focus the beam, so the smallest length that the geometric limitations allowed in the test-bay, $\ell = 372$ mm, was used in all the scans. In order to minimize beam scattering at the surface and thus improve the vibrometer signal-to-noise ratio, the rail surface was lightly brushed with sandpaper.

A scan of point P_3—the point at the middle of the top of the cross-section (see Fig. 4)—was also completed in order to confirm that vertical displacement during lateral excitation is indeed negligible. Only a general idea of the vertical displacement amplitudes was needed for this study, so the calibration and noise data were not measured for the P_3-scan. In order to scan the point P_3 perpendicularly to the top of the rail, the laser beam was deflected at 90° by a $\frac{1}{2}$ in-diameter broadband dielectric mirror (400–900 nm range). The mirror was fixed on a mirror mount that

could slide on the horizontal 'arm' attached to the bracket, which could slide vertically along the same post that carried the vibrometer fixture.

3.3. Signal processing, calibration and noise

A single 12-bit National Instruments DAQCard™-6062E in an IBM ThinkPad PC was responsible for generation of the continuous sine waveform at frequency f, and for simultaneous acquisition and digitization of the waveforms detected by the laser vibrometer and the accelerometer. Generation and acquisition were controlled in separate virtual instruments (VI's) in National Instruments LabVIEW 6.1 software. The single frequency sine waveform generated in the DAQCard was amplified in a Crown® DC-300A II dual-channel power amplifier, which then provided the input current for the electrodynamic shaker. A general schematic of the generation and the acquisition part of the measurement setup is shown in Fig. 5.

According to Shannon's sampling theorem [11], the signal must be sampled at a rate at least twice the highest frequency of the signal—in the present case, the excitation was at a fixed frequency in the 200 ± 3 Hz range, so the vibrometer and accelerometer signal capture rate of $2^{13} = 8192$ samples/s (or $\delta t = 1/8192 = 1.22 \times 10^{-4}$ s for each sample) was deemed sufficient. Because 2s of data were taken at each scan point, a total of $N = 16384$ samples were recorded.

In order to minimize the influence of noise, each waveform was then filtered by a digital lock-in technique at the known frequency of vibration, $\omega = 2\pi f$. This frequency was set by the operator from the waveform generator VI on the PC and is known with virtually perfect precision. The lock-in process converts the record $\boldsymbol{v}_i(t)$ of the vibrometer signal, captured over a period of time T,

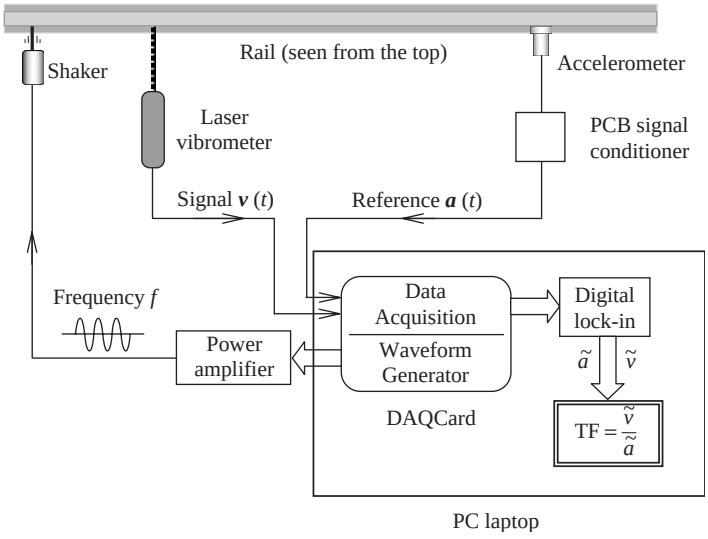

Fig. 5. Schematic of signal processing (output is the transfer function at particular z).

to a single complex number, its complex amplitude:

$$\tilde{v} = \sum_{n=0}^{N-1} v_n e^{-i\omega t_n} = \sum_{n=0}^{N-1} v_n e^{-i\omega n\delta t} \approx \frac{1}{\delta t}\int_0^T \boldsymbol{v}(t) e^{-i\omega t}\, dt, \tag{6}$$

where v_n is the recorded voltage at time $t_n = n\delta t$. The complex amplitude $\tilde{a}$ of the accelerometer signal is given by a similar expression. If the duration of capture T is an integer multiple of the vibration period $2\pi/\omega$, the above is an element of the discrete Fourier transform [11,12]. In general, however, such commensurability does not obtain.

This lock-in process is recommended for the usual reasons—it filters out the effect of signal noise. For illustration, consider a case in which $\boldsymbol{v}(t)$ is a sinusoid plus noise. At time t_n, it is

$$v_n = \cos(n\omega\delta t + \phi) + \vartheta_n. \tag{7}$$

The lock-in procedure yields

$$\tilde{v} = \frac{N}{2} e^{i\phi} + \tfrac{1}{2} e^{-i\phi} \frac{\sin(N\omega\delta t)}{\sin(\omega\delta t)} + \sum_{n=0}^{N-1} \vartheta_n e^{-i\omega n\delta t}. \tag{8}$$

The numerator of the second term depends on the commensurability of $T = N\delta t$ and ω, but its maximum absolute value is 1, and the term is therefore negligible. The third term is random; its root-mean-square (rms) is smaller than the magnitude of the first term by a factor of order $2\,\mathrm{rms}(\vartheta_n)/\sqrt{N}$. Large N leads to relatively small contamination of the output by the noise.

The lock-in has another useful feature—it filters out extraneous frequencies (noise, or harmonics induced by nonlinearities in the shaker or in the detectors). A simple calculation shows that the contribution of a frequency $\alpha \neq \omega$ is attenuated by a factor of the order $T(\alpha - \omega)$. Thus a harmonic 2ω is attenuated in practice (where $\omega/2\pi \approx 200\,\mathrm{Hz}$, and $T = 2\,\mathrm{s}$) by a factor of about 2500.

The ratio of the filtered vibrometer signal to that of the accelerometer signal is the measured complex transfer function [13]

$$TF = \frac{\tilde{v}}{\tilde{a}}. \tag{9}$$

That the transfer function is defined in this way allows the procedure to accommodate vagaries in the response of the structure. Shaker electronic impedances are notoriously sensitive to temperature; even when run at a constant input voltage, the force produced by a shaker is a function of current, which is in turn a function of both voltage and impedance. Hence, the response of the structure can vary in the course of the scan. As shown in a more detailed study [9], such drifts are undesirable.

The signal processing concludes with a record of the complex TF at each of the many laser vibrometer scan positions. Finally, the scanned displacement profile is

$$d(z) = C\,\mathrm{TF}(z), \tag{10}$$

where C is a constant that can be obtained from the laser vibrometer output calibration specifications for the particular vibrometer settings, but is irrelevant for this application because it drops out in the fit process.

Measurements of the force, using a force transducer between the shaker and the rail, and the use of the more conventional definition of transfer function frequently used in vibration testing [10], $\mathrm{TF} = \tilde{v}/\tilde{s}$, where $\tilde{s}$ is filtered force transducer signal, could in principle compensate for variations in the response mentioned above. However, the measurement of acceleration from a fixed accelerometer is preferred for present purposes. Small variations in the structure itself (e.g., due to temperature fluctuations) can lead to variations in the overall response of the structure that would not be compensated by the ratio $\tilde{v}/\tilde{s}$. This is especially true if the structure is driven near a resonance where its response is particularly sensitive to external parameters, which is the case in the present measurements.

Although the chosen definition of transfer function (9) ensures that most of the instrumentation drift is filtered out, some drift still shows in the data and it is ascribed to the laser vibrometer and accelerometer being intrinsically different instruments, with different calibration sensitivities to ambient temperature. The character and the magnitude of this transfer function drift were examined by fixing the laser vibrometer at one point on the rail and recording the response (2 s of data) at that point, every 10 s over a period of 160 min while the rail was being excited laterally at a frequency of 233 Hz.

As seen in Fig. 6, the amplitude of the transfer function (with the mean = 64.4) drifted by –0.7 (i.e., 1%), while the phase (with the mean = 0.629) drifted by 0.004 rad. The redeeming characteristic of the drift is its apparent linearity, certainly over any 30 min range. Although the drift was relatively small, it was considered necessary to calibrate the output with respect to it, using its linearity feature.

Several measurements were taken at a chosen fixed point (one with a generally high response) before and after each scan—such measurements will be referred to as 'point-scans'. They were used for the calibration of drift and for noise estimates.

In order to ensure absolute referencing, it is important that both point-scans are taken at exactly the same point. In the test-bay measurements a point at $z = 31$ cm on the P_2-scan line (on the web of the rail) was selected for the calibration reference. The means of the two sets (per each scan) were termed 'calibration before' c_{bfr} and 'calibration after' c_{aftr}, and were used to obtain the slope of the drift that may have occurred during the scan. Each point of the scan was then corrected for the appropriate amount of drift according to the calibration equation

$$d(z) = \mathrm{TF}(z)\frac{c_{\mathrm{bfr}}}{c_{\mathrm{bf}r} + (c_{\mathrm{aftr}} - c_{\mathrm{bfr}})z/L_s}, \tag{11}$$

where $\mathrm{TF}(z)$ is the complex transfer function for the entire scan, L_s is the total scan length, and $d(z)$ is the calibrated measurement—also a complex function. Both the P_1- and P_2-scans were calibrated according to this equation, prior to being used in the χ^2 fit.

The signal noise for each scan was estimated using similar point-scans, but in this case the fixed point was associated with a particular scan, again at $z = 31$ cm. The measure of noise was the variance of point-scan data for each scan, $\sigma^2_{P_1}$ and $\sigma^2_{P_2}$, respectively. In practice, they were approximately equal.

Processing of calibration and noise data was then completed within a fit code written in Mathematica 4.2 software.

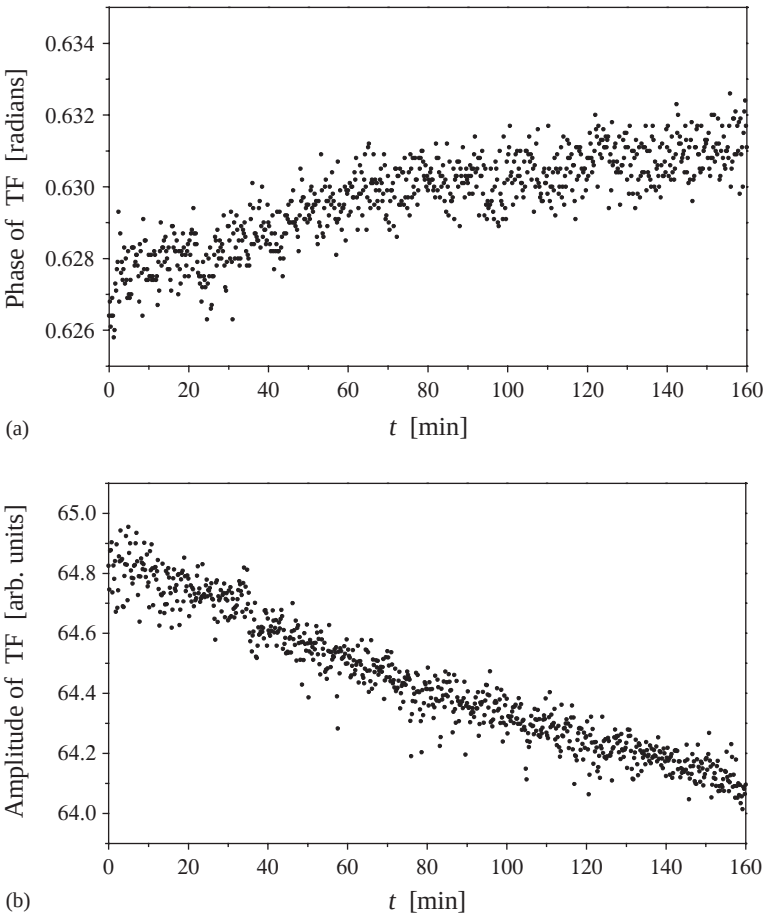

Fig. 6. (a) Phase and (b) amplitude of the transfer function drift.

3.4. Resonant frequency measurements

One of the important requirements of the proposed technique is a high signal-to-noise ratio. It is usually achieved by choosing the driving frequency at or near a resonance in order to provide a high amplitude of response. A long wavelength (~4 m) resonance was found at about 60 Hz, with a bow-like mode shape. Better fits were obtained, however, and strong responses, for a sine-like mode shape in the vicinity of 200 Hz, at a wavelength of about 2 m.

However, resonant frequencies are very sensitive to changes in the system—change in rigidity due to change in load, slight shifting of supports during loading, changing the positions of attachment of shaker and accelerometer, etc. Because the resonant frequency peaks in the frequency spectrum of this system are very sharp, with about 1 Hz width, driving the rail at a frequency slightly lower or higher than the exact resonant frequency naturally results in a considerably weaker response [10]. It was, therefore, considered beneficial to measure the exact resonant frequency of the desired mode prior to the measurements at each load level. (The shaker and the accelerometer were kept in exactly the same position for all scans.)

The desired frequency was obtained by modal testing of the rail in the particular setting. The same instrumentation was used as for vibration scans, but the excitation was transient instead of steady-state—a light tap on the rail, with a plastic hammer and in the lateral direction. The laser vibrometer was aimed at the presumed location of maximum response and recorded 10 s of data that was then Fourier-transformed. A peak in the frequency spectrum corresponds to the desired natural mode.

This procedure is illustrated on the case of the rail before its ends were cut and polished for the measurements under load, and with slightly different placement of the shaker and accelerometer. As seen in Fig. 7, slightly less than 7 s of data were taken, enough to obtain a clear frequency spectrum, with a very sharp, obvious peak at 227 Hz. (An overbar denotes a Fourier-transformed

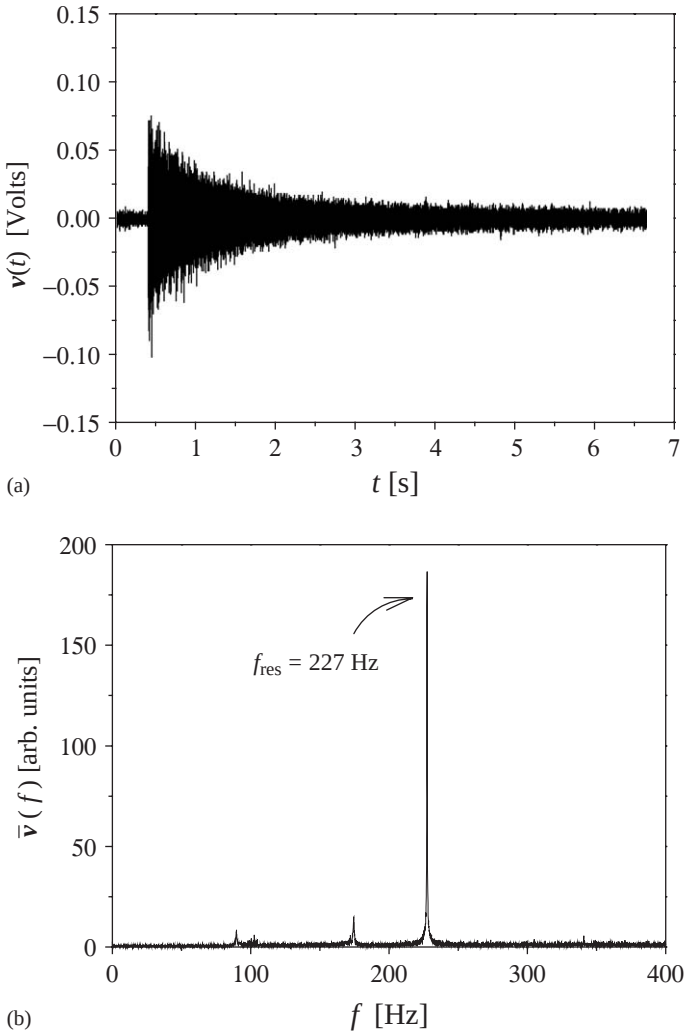

Fig. 7. Results of modal testing of uncut (93 in long) rail with no load: (a) response and (b) frequency spectrum.

variable.) The amplitude of the rail response, then, while driven at this frequency, was high, with excellent signal-to-noise ratio.

This modal testing was employed before the scans at each load level. The difference in frequencies of the natural mode of interest, for different loads in the range used in this study (0–100 kips), were small, as seen in Fig. 8.

The value corresponding to zero load was omitted from the plot simply because the boundary conditions for that case are quite different than those for the case of the loaded rail. The trend is otherwise an increasing one and it contradicts the implications of the Euler–Bernoulli beam theory that the increase in compressive load should correspond to a decrease in natural frequency. Livingston et al. [6] used the same theory, but with translational/rotational spring supports on both ends—they measured several of the lowest resonances and fit them to the theory by varying load and end stiffness. Their measurements, also at known load, have shown that the slope is positive, as in the present study. It is perhaps not surprising that a model of spring supports whose stiffnesses do not vary with load fails to describe real systems. This result illustrates how natural frequency data as a source of information about contained stress are unreliable.

3.5. The least-squares fitting procedure

The data was fit to theoretical expectations by minimizing the following least-squares residual:

$$\chi^2(\alpha_{1\ldots5};\ \delta,\delta z) = \frac{1}{N_z}\left(\frac{1}{\sigma^2}\sum_{i}^{N_z}\left|d_1(z_i) - \hat{d}_1(z_i,\omega;\ \alpha_{1\ldots5};,\delta z)\right|^2 + \frac{1}{\sigma^2}\sum_{i}^{N_z}\left|d_2(z_i) - \hat{d}_2(z_i,\omega;\alpha_{1\ldots5};\delta,\delta z)\right|^2\right), \tag{12}$$

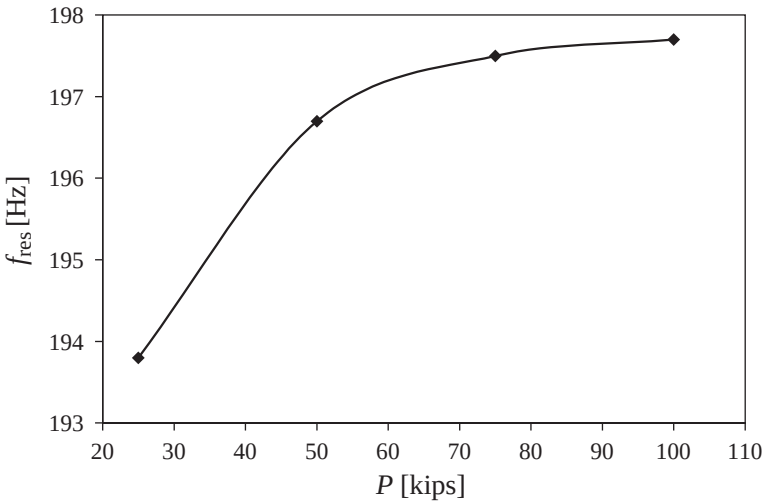

Fig. 8. Resonant frequencies for the $91\frac{3}{4}$ inch long rail 136-lb AREMA, for four different loads.

where $\hat{d}$ is taken in the form (4) of a sum of rightward and leftward waves. The sum is confined to 5 waves in each of the two directions: the lateral bending wave, the torsional wave, the evanescent lateral bending wave, and two less well known evanescent waves whose importance is confined to regions near supports and loads, but whose influence could not be neglected. The vertical bending waves and the extensional wave have been neglected, consistent with expectations (the loading does not excite them efficiently, and the measurement is relatively insensitive to them) and consistent with rough measurements on the top of the rail (see below).

The minimimzation is taken with respect to the α_m's, and may be constructed in closed form, as the regression in those variables is linear. Further minimization with respect to two additional nonlinear parameters is also conducted. One such is δz (described below). The chief parameter is δ, which describes how the wavenumbers are distorted:

$$\tilde{k}_m = \begin{cases} k_m & \text{if not lateral bending,} \\ k_m(1+\delta) & \text{if prop. lateral bending,} \\ k_m(1-\delta) & \text{if evan. lateral bending.} \end{cases} \tag{13}$$

Section 4 shows the best fit values of δ and δz as extracted from this process, and also shows the actual residuals, $d_1(z_i) - \hat{d}_1$.

3.6. Extraction of contained load

As explained above, the main assumption is that the change in $k_{\text{lat.bend.}}$ due to contained load, as calculated using Euler–Bernoulli beam theory, is the same as the change in $k_{\text{lat.bend.}}$ obtained in the test-bay measurements at known load. This assumption is illustrated in the sketch of a lateral bending branch in the rail dispersion graph (Fig. 9). This distortion of $k_{\text{lat.bend.}}$ due to contained load P is easily calculated from the Euler–Bernoulli beam theory, starting from the dispersion

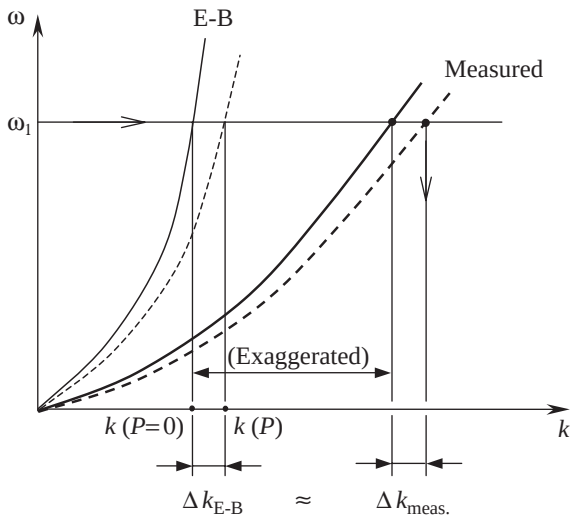

Fig. 9. Sketch of the lateral bending branch of dispersion relation for several cases: the Euler–Bernoulli beam theory and the measurement, with and without load (full and dashed lines, respectively).

relation (1):

$$\left.\frac{\delta k}{k}\right|_P = \frac{1}{4A\rho c_b^2 r_g^2} \cdot \frac{P}{k^2}, \tag{14}$$

where $\delta k/k$ is the relative distortion of $k_{\text{lat.bend.}}$ (or just δ) and δk is $k^{\text{measured}}|_P - k^{\text{FEM}}|_{P=0}$. For the load range of 0–100 kips, the $P(\delta k/k)$ curve defined by Eq. (3) is linear, passing through the origin. Its slope, for the rail 136-lb AREMA, is 0.01 %/kip. That is the curve that would be used in the field to estimate the contained load for a known distortion of $k_{\text{lat.bend.}}$, obtained from the measurement fit.

4. Measurement results

4.1. Measured displacement profile

All the displacement profiles shown in this subsection are the raw, uncalibrated, measurement data (that is, the transfer function), as represented by Eq. (10)—the calibrated data have the same appearance and features as the raw data. The difference between the raw and calibrated data is barely noticeable on the graph with a scale including the full response range.

The following representative graphs illustrate the typical displacement measurements obtained in all cases. The real and imaginary parts of the measured lateral displacement of point P_1 on the side of the rail head, at zero load and excited at a frequency of 203.1 Hz, are shown in Fig. 10. The apparent wavelength, calculated from the figure as twice the peak-to-peak distance, is 80 in, which is close to the predicted wavelength of the lateral bending mode—78 in—indicating that the response is, indeed, dominated by the lateral bending. The shape of the response curve was qualitatively the same at all load levels.

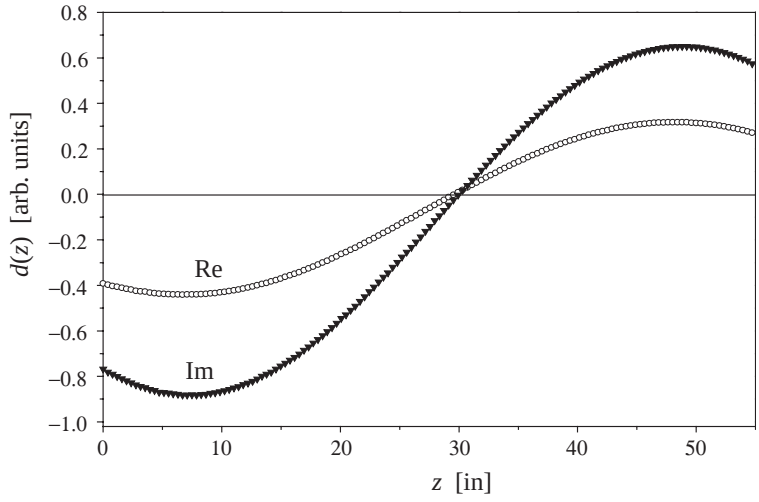

Fig. 10. Lateral displacement measured in the P_1-scan (across the side of the rail head).

It is interesting to note that the peaks of the real (Re) and imaginary (Im) part are almost in phase. The slight shift is best noticed at the point where Re and Im curves cross—that point is slightly removed from the $d = 0$ axis. The phenomenon is due to a slight contamination of the wave field by travelling components—the field is not a purely standing wave; there are losses at the supports.

On a single curve, Re for example, it can also be seen that the absolute magnitudes of the peaks are not equal. This result is again due to the influence of the torsional mode: the lateral displacements of the bending mode are almost the same for those positions, but the lateral components of the torsional displacement are not. When they are added within the sum of modes, the total magnitudes of the response for those two z positions are different. For the same reason, the ratio of the peak magnitudes for the P_1-scan is not the same as that for the P_2-scan (see Fig. 11).

Important additional information regarding the influence of the vertical bending waves on the measurement is revealed with closer scrutiny of the response curves. The magnitude of vertical displacement during lateral excitation was measured by scanning the point P_3 on the top of the rail head. Comparison of the Re curves of the P_1- and P_3-scans confirms the assumption that the contribution from the vertical bending is negligible. It can be seen in Fig. 12 that the maximum amplitude of the P_3-scan is about $1/C_1 = 10$ times smaller than that of the P_1-scan. It can also be seen that the wavelength of the P_3-scan is close to that of the lateral bending mode, indicating that the lateral bending mode is dominant and the influence of vertical bending is very small, i.e., of the order $C_2 < 1$. Finally, the lateral displacement component of the vertical bending mode is also very small, again at least of the order $C_3 < 1$. Together, these three arguments lead to conclusion that the overall contribution of the vertical bending mode to the lateral displacement due to lateral excitation is of the order $C_1 C_2 C_3 \ll 1$, confirming that the vertical bending mode may be neglected in the fits.

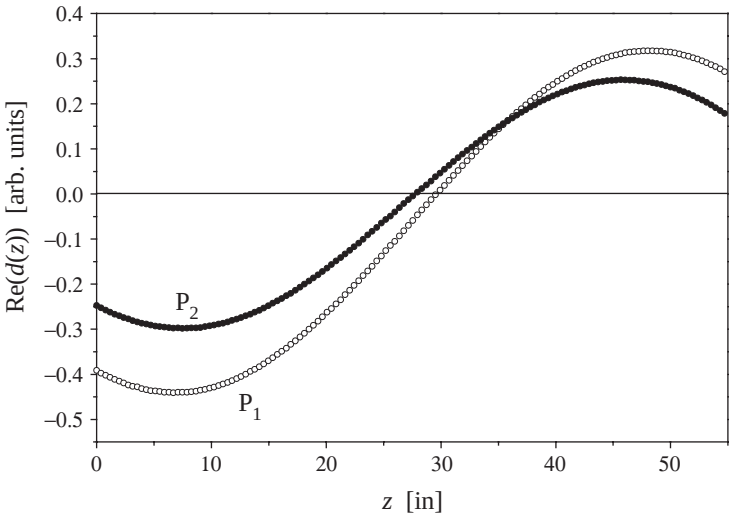

Fig. 11. Comparison of lateral displacements in the P_1- and P_2-scans (P_1 is on the side of the rail head, P_2 is on the rail web).

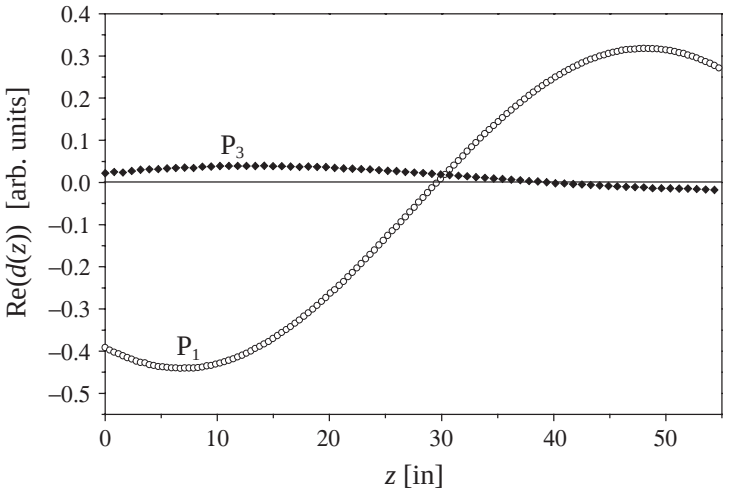

Fig. 12. Comparison of the magnitudes of vertical and lateral displacement due to lateral vibration. (P_1 is on the side of the rail head, P_3 is on the top of the rail head.)

4.2. Fit residuals as indicators of measurement errors

For each load case the best-fit residuals [14] were plotted and examined for irregularities that would indicate errors in the measurement. In all cases, the residuals are small compared with the data itself, thus indicating good fits. In some cases the residuals showed systematic trends, indicative of measurement errors, which could be corrected by modifying the fit procedures.

If a z-position was accidentally missed or repeated in the scan, it appeared in the plot of the residuals as a shift of part of the curve, starting from the offending position. This type of operator-induced error occurred in only 3 out of 24 scans, and it was easily corrected by shifting the entire curve by one point in the appropriate direction. Another easily corrected error was due to occasional random glitches in the electronics. Its manifestation was a spike in the plot of the residuals. Such data points never occurred more than once in any scan (in most scans not at all), and were simply excluded from the fit.

The residuals of the raw data had a similar trend but higher magnitudes than those of the calibrated data, thus confirming the need for calibration. Although the drift as a sole source of measurement error has a small influence on distortion of $k_{\text{lat.bend.}}$, if combined with other measurement errors (as it was the case in the test-bay) it contributes to the overall inaccuracy. Since the drift is one of the errors that can be adequately compensated for, the calibration for drift was completed for all scans. An example of error introduced through calibration itself is shown in Fig. 13. A simple case of contamination with a large wavelength error introduced through erroneous calibration was detected in the 75 kips data. Upon correction of the calibration, the fit residual acquired usual appearance, with fluctuations mostly due to random noise.

One measurement error that occurred in all tests was a kink in the horizontal alignment of the scan. It is illustrated here in the zero-load case. The residual of the best-fit displacement of the P_2-scan has a distinct jump around the middle of the scan region, as seen in Fig. 14. Such jumps in

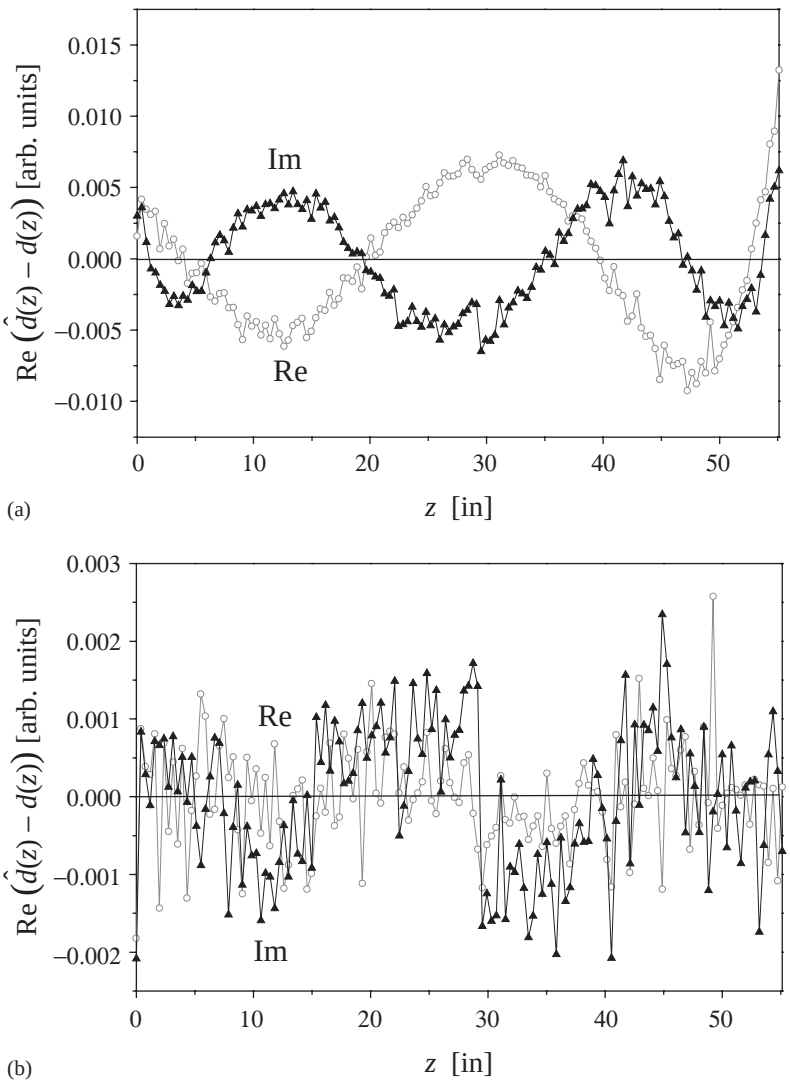

Fig. 13. Residuals of the data contaminated by (a) miscalibration and (b) after correction.

other cases also occurred around the middle of the scan. Careful consideration of all the physical activities of the operator, as well as the instrumentation condition during the scan, identified the culprit: the brief readjustment of seating when scanning around the middle of the range, in order to make the manual moving of the heavy laser assembly easier, interrupted the otherwise smooth process, so moving the laser to the next few positions included the temporary kink. Preliminary lab measurements over the shorter scan regions that required no rearrangements of operator's position, had no jump in the fit residues, which confirms the above explanation. Because this error occurred in all the scans, it was considered appropriate to exclude a few middle points from the fit. The total number of points excluded around the middle of the scan region was between 5 and 14

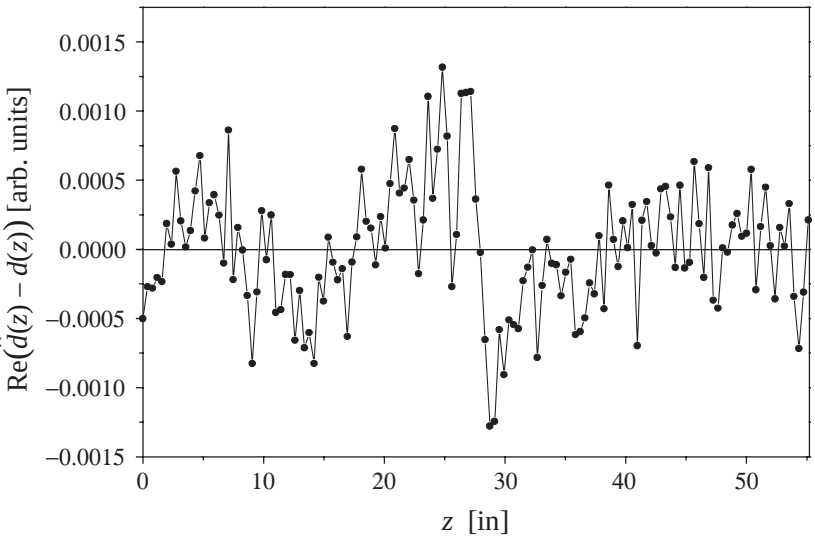

Fig. 14. Fit residual for the P_2-scan indicating the occurrence of the kink in the middle of the scan range.

for all the scans—it is a small number compared with 141 points in a full scan, and the decrease in the fit accuracy (χ^2) because of fewer fit points was a minor effect compared with the increase of accuracy due to 'cleaner' data.

The random fluctuations in residuals that are larger in the vicinity of the places where the data itself is small, indicate that there are random fluctuations in z. Such fluctuations (of typical magnitude δz) translate to residual fluctuations of typical magnitude $\delta z(\mathrm{dTF}/\mathrm{d}z)$, which have a fractional size of order $\delta z \cdot k_{\mathrm{lat.bend.}}$, and more characteristically, are the greatest where TF has the greatest slope with respect to z, i.e., at the zeros of the TF. On observing such fluctuations in the residuals, one concludes that there are random z errors, and that they lead to somewhat greater 'noise'—albeit correlated with zeros of TF. Therefore, they are not of great concern.

The possibility that there is a z-shift between the P_1 and P_2 scans leads to a residual of characteristic shape. Our design of the scan apparatus neglected to control against such errors. One key feature of this kind of error is that the residuals of P_1 and P_2 data will be equal and opposite; one will be the negative of the other. The other feature is a shape of the residual resembling capital letter M (or W). The amount of mismatch in the scan origin between two scans is estimated to be of order $\delta z = \varepsilon / k_{\mathrm{lat.bend.}}$, where ε is the fractional size of the residual fluctuations. This quantity was calculated for all the cases and it amounted to not more than 0.049, 0.086, 0.05 and 0.062 in, for loads of 100, 75, 25 and 0 kips, respectively.

The fit procedure was constructed to allow for slight differences of the scan origin between the P_1 and P_2 scans—an additional nonlinear parameter δz was justified by the improved fits. Best-fit values for this shift of scan origin were 0.005, 0.028, 0.07 and 0.035 inches, respectively, and are in qualitative agreement with the amounts estimated above.

4.3. Contained axial load

After removal of the kink-affected points in the middle of the scan range, the best-fit amount of distortion of $k_{\text{lat.bend.}}$ ($\delta k/k$, or simply δ) for the 4 load cases was plotted versus applied load P. The graph is shown in Fig. 15.

The slope of the linear fit through those points is $s = 0.00983\,\%/\text{kip}$, which is approximately the same as the expected $0.01\,\%/\text{kip}$. Most critically, as seen in Fig. 16, the root-mean-square fluctuation of the $P(\delta)$ data points from the linear fit (i.e., the deviation from the zero residual) is 0.0105%, far better than the target precision of $k_{\text{lat.bend.}}$, 0.27%.

Considering that in the proposed technique the slope is the key to contained load, the value obtained in the measurements bodes well for the success of the technique in the field. It is even more noteworthy that the measurement points do not deviate substantially from the linear fit. A large deviation would indicate that more modes should be included in the sum, or that some important mode was neglected, or that some other uncontrolled and erratic error was playing a role in the measurement procedure.

A missing 50 kips data point is somewhat disconcerting, but could not be avoided. That the measurements at 50 kips contained significant errors was noticed only after the setup was disassembled, and they could not be repeated.

While the slope is in excellent accord with expectations, the linear fit does not pass through the origin as expected, but rather intercepts the δ axis by the amount of $\varepsilon = 0.36\%$. A simple analysis shows that, for a nonzero ε, the error in an estimate of P would be ε/s. For $\varepsilon = 0.36\%$ the load imprecision amounts to 36 kips, which is higher than the target load accuracy of 26 kips.

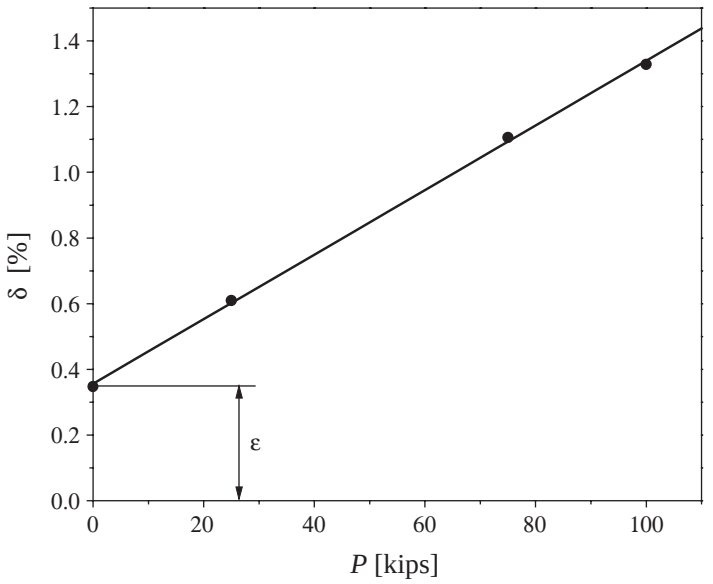

Fig. 15. Applied load versus relative distortion of $k_{\text{lat.bend.}}$ The best-fit line, $\delta = sP + \varepsilon$, has the slope $s = 0.00983\%/\text{kip}$ and the intercept $\varepsilon = 0.356\%$.

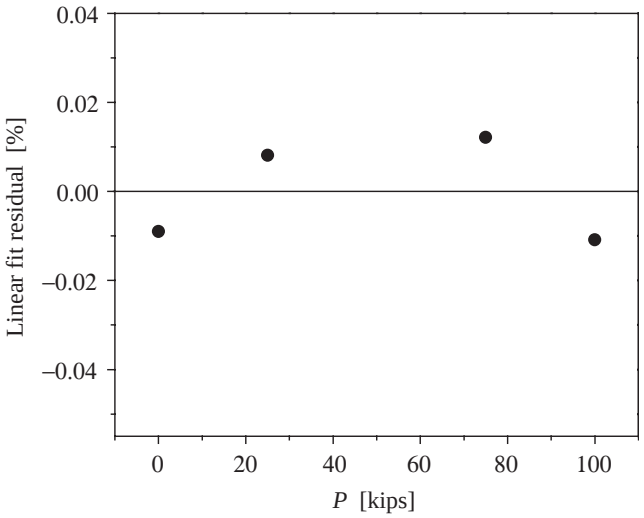

Fig. 16. Residual of the linear fit of $P(\delta)$. RMS = 0.0102%.

Although it is possible that the intercept was due to some general parameter having the same error for all the load levels in this regime, it is speculated here that ε represents an error in our estimates of geometry of the cross-section. The cross-section outline used in FE solution was not an exact copy of the outline provided by the commercial rail specifications, which in turn is also not a perfect representation of the outline of the rail that was used for the measurements. In situ profilometry of the cross-section—a standard procedure commonly used in the field—would resolve this problem, but it was not available for the measurements described here. In cases when the material properties or geometry cannot be reliably determined, the procedure could be modified to include an additional set of two scans at a different frequency—the output of the fitting procedure would in that case be the load and reference rigidity *EI*.

It is also worth mentioning that in some cases the bounds of the kink-affected region were not clear, so each point shown on Fig. 15 has its own error bar, or rather, a variation of δ due to somewhat arbitrary manual selection of the middle points to be excluded from the fit. The points shown here were obtained with a conservative selection of the middle range to be excluded. If no kink-affected regions are excluded from the fit, the resulting $P(\delta)$ has a slope of 0.0106 %/kip and an intercept of $\varepsilon = 0.785\%$. A more detailed statistical analysis of the variations in slope of $P(\delta)$ was deemed outside the scope of this work.

5. Conclusions

We proposed a new non-destructive vibration technique for the in situ nondestructive measurement of longitudinal stress in railroad rails. Its underlying principles are simple: that such stress affects the wavelength of bending waves, and that the wavelengths can be inferred by

comparing the vibration amplitude distributions with distributions based on the wavenumbers obtained from elastic waveguide theory. In practice, the technique was found to require a high precision finite-element code for prediction of wavenumbers, to require an elaborate fitting procedure with careful attention to the presence of both propagating and evanescent-guided modes, and to require careful attention to sundry potential sources of systematic measurement error. This technique can be applied to any slender structural element under static axial load, and for the particular technologically pressing case of railroad rail, the technique was found to be viable.

Two chief sources of error relevant to the proposed measurement technique were recognized. Intrinsic beam properties (as represented by c_b and r_g in Eq. (1)) and vibration response (as represented by the $k_{\text{lat.bend.}}$) each must be known with sufficient accuracy.

The lateral bending wavenumber has been extracted with high precision (as seen in the small residuals of the $P(\delta)$ linear fit in Fig. 16)—a precision 25 times greater than had been targeted was achieved using a moderately fine mesh and entirely manual alignment and scanning. With this in mind, vibration measurement errors are no longer critical to a successful development of the technique.

However, it was also found that the intrinsic rail properties (as represented by the predicted wavenumber at zero load) have not been obtained with the same accuracy. The error is not in the FEM code, considering that $k_{\text{lat.bend.}}$ has converged well. The values for c_b and c_L, as obtained ultrasonically, were also highly accurate. The obvious inference is that the rail shape was the culprit. As seen in Eq. (2), a 0.71% error in the effective r_g would suffice to explain the remaining errors. A rough comparison of the standard rail shape and the mesh perimeter of the modified version used in the FEM code indicates that there is a difference of similar magnitude. A detailed quantitative comparison was not undertaken.

It is remarkable that the rather sloppy apparatus nevertheless allowed sufficient precision in the recovered values of $k_{\text{lat.bend.}}$. This was, however, at large cost in operator fatigue, in a posteriori error corrections, and in general uncertainty. Therefore, there remains the need for an improved apparatus that would allow more efficient test and fit procedures. At the cost of sacrificing some measurement precision, a practical test could be conducted with much greater speed just by taking less than 2 s of data per point, as signal-to-noise ratios appear to be much better than necessary.

The remaining issue most critical for a viable practical technique remains an accurate a priori estimate of the zero-stress wavenumber. This appears to be a matter of making accurate measurements of the rail shape. Alternatively it may be possible to make measurements of wavenumbers at more than one frequency, thereby determining both load and reference rail properties. If the issue of rail shape measurement can be addressed, then we have a technique that promises to be sensitive to contained load and, most importantly, does not require modelling or measurement of supports. It is a technique that neither requires a zero-state reference measurement, nor is sensitive to residual stress or microstructure.

As discussed following Eq. (2), the requirements on accuracy in lateral bending wavenumber, both for the reference and measured k, are much reduced if measurements can be made at lower frequency, the cost being the need to unfasten more ties. The issue that remains therefore is to determine what optimal span of rail will most efficiently and accurately recover neutral temperature.

6. Guidelines for further development

The method's good accuracy confirmed in the test-bay is promising for its further implementation in the field. Several issues that could readily be resolved were identified in the course of development of the method.

The use of an automatic high-precision laser platform and alignment procedure would improve the displacement measurement precision and remove the need for adjusting the scan origins analytically in the fit procedure. It would also minimize the kink, and other errors stemming from inadequate alignment of the laser. This improvement would be a necessary first step in technique development for commercial applications.

The previously mentioned profilometry would add a relatively brief step to the in situ measurement procedures; the necessary tools are already in use by the rail maintenance crews. The use of profilometry would also require the on-site calculation of $k_{\text{lat.bend.}}$.

Finally, replacing the accelerometer with another laser vibrometer, for a finer referencing signal without a drift due to calibration sensitivity mismatch, would provide more accurate measurement without the need for calibration of every scan, and it would also decrease the processing time considerably.

In conclusion, the proposed laser vibrometry technique for measuring the contained longitudinal stress in slender structural elements was proven accurate in the test-bay measurements with a known load. With several reasonable equipment upgrades, it can be improved to become a reliable and portable tool for in situ stress measurements.

Acknowledgements

This work was supported by the Technology Scanning Committee of the Association of American Railroads and the Transportation Research Board's High Speed Rail IDEA program. The National Computational Science Alliance provided resources on its Silicon Graphics Origin2000. The Newmark Structural Engineering Laboratory at the University of Illinois at Urbana Champaign provided the testing facilities.

References

[1] A.M. Zarembski, On the nondestructive in-track measurement of longitudinal rail force, Technical report, R-406, of the Association of American Railroads, Chicago IL, 1980.

[2] O. Orringer, J. Orkisz, Z. Swiderski (Eds.), *Residual Stress in Rails; Effects of Rail Integrity and Railroad Economics, Proceedings of a conference at the Cracow Institute of Technology*, vols. I, II, Kluwer, Boston, 1992.

[3] Y.H. Pao, W. Sachse, H. Fukuoka, Acoustoelasticty and ultrasonic measurements of residual stress, *Physical Acoustics* XVII (1984).

[4] H.D. Harrison, T.O. McCanney, L.L. Doll, Wayside system for measuring rail longitudinal force due to thermal expansion of continuous welded rail, *SPIE Proceedings* 2458 (1995) 225–231.

[5] A. Kish, S. Kalay, A. Hazell, J. Schoengart, G. Samavedam, Rail longitudinal force measurement evaluation studies using the track loading vehicle, *American Railway Engineering Association Bulletin* 742 (1993) 315–342.

[6] T. Livingston, J.G. Béliveau, D.R. Huston, Estimation of axial load in prismatic members using flexural vibrations, *Journal of Sound and Vibration* 179 (5) (1995) 899–908.
[7] T.P. Boggs, J.G. Béliveau, T.M. Murray, Determination of axial load and support stiffness of continuous beams by vibration analysis, AAR Research Report No. CE/VPI-ST 94/14, 1994.
[8] V. Damljanović, R.L. Weaver, Forced response of a cylindrical waveguide with simulation of the wavenumber extraction problem, *Journal of the Acoustical Society of America,* in press, 2004.
[9] V. Damljanović, R.L. Weaver, Propagating and Evanescent Elastic waves in cylindrical waveguides of arbitrary cross section, *Journal of the Acoustical Society of America,* in press, 2004.
[10] D.J. Ewins, *Modal Testing: Theory, Practice and Application*, second ed., Research Studies Press, Baldock, England, 2000.
[11] D.J. Inman, *Vibration: With Control, Measurement and Stability*, Prentice-Hall, Englewood Cliffs, NJ, 1989.
[12] D. Schlichthärle, *Digital Filters—Basics and Design*, Springer, Berlin, 2000.
[13] A.D. Pierce, *Acoustics—An Introduction to Its Physical Principles and Applications*, McGraw-Hill Series in Mechanical Engineering, McGraw-Hill, New York, 1981.
[14] S.G. Rabinovich, *Measurement Errors and Uncertainties—Theory and Practice*, second ed., Springer, New York, 2000.